Journal of Constructional Steel Research 67 (2011) 360–378

Contents lists available at ScienceDirect

Journal of Constructional Steel Research

journal homepage: www.elsevier.com/locate/jcsr

Behaviour of short and slender concrete-filled stainless steel tubular columns

Brian Uy [a], Zhong Tao [a,b,*], Lin-Hai Han [c]

[a] School of Engineering, University of Western Sydney, Penrith South DC, NSW 1797, Australia
[b] College of Civil Engineering, Fuzhou University, Fuzhou, Fujian Province, 350108, China
[c] Department of Civil Engineering, Tsinghua University, Beijing, 100084, China

ARTICLE INFO

Article history:
Received 7 May 2009
Accepted 22 October 2010

Keywords:
Concrete-filled steel tubes
Stainless steel
Short columns
Slender columns
Axial compression
Eccentric loading
Strength
Design

ABSTRACT

In this paper, a series of tests were carried out on short and slender concrete-filled stainless steel tubular columns to explore their performance under axial compression or combined actions of axial force and bending moment. Empty short steel hollow sections were also tested for comparison. The test results showed that the performance of the composite columns was quite good and have the potential to be used extensively as structural members. Comparisons of the test results were also made with several existing design methods for conventional concrete-filled carbon steel tubular columns as presented in Australian standard AS 5100 (2004), American code AISC (2005), Chinese code DBJ/T 13-51-2010 (2010), and Eurocode 4 (2004), which indicates that all the codes are somewhat conservative in predicting the load-carrying capacities of both short and slender columns.

1. Introduction

Stainless steel has been used in the construction industry for some years as minor components, such as fixings, fasteners, and cladding [1,2]. The initial high cost, however, has greatly limited its structural use. In recent times, the whole-life cost for a structure has become an important concern for developers, contractors, architects, engineers and property owners. Owing to the benefits of stainless steel, it is believed that this steel material will be increasingly used in civil engineering and construction. This has been recently witnessed in a lot of projects around the world [2,3].

To make more economical use of stainless steel, it is advisable to fill stainless steel hollow sections with concrete to develop an innovative composite construction technology. The success of this new technology has been demonstrated by tests carried out by Young and Ellobody [4] and Lam and Gardner [5], where 14 and 12 stub column test results were reported in [4,5], respectively. Since the material behaviour of stainless steel is quite different from that of conventional carbon steel [6], it seems that further experimental and numerical investigations are needed to investigate the behaviour of concrete-filled stainless steel tubular (CFSST) columns before developing rational design guidance. This paper presents a comprehensive experimental investigation on short and slender concrete-filled steel tubular (CFST) columns where stainless steel material was used to fabricate the outer jackets. Further numerical simulations will be presented in companion papers.

In the test program, a total of 60 tests were carried out on short CFSST columns to explore their performance under axial compression or the combined actions of axial force and bending moment. Thirty three short empty stainless steel hollow sections were also tested for comparison. Meanwhile, tests on 24 composite columns comprised of stainless steel were conducted with an aim to investigate the performance of slender CFSST columns. Several existing design codes, including the Australian design code AS 5100 [7], American code AISC [8], Chinese code DBJ/T 13-51-2010 [9] and Eurocode 4 [10], are used to predict the column strength and to compare with the test results. These codes are to be referred to as "AS 5100", "AISC", "DBJ/T" and "EC4" in the following.

2. Experimental investigation

2.1. General

An experimental program involving a total of 117 specimens has been carried out. The test specimens were classified into four different groups: Group I: 72 short columns under axial compression; Group II: 9 short columns to investigate the influence of different loading methods; Group III: 12 short beam–columns under axial compression combined with bending; and Group IV: 24 columns under axial compression to investigate the influence of slenderness. Circular and square specimens as shown in Fig. 1(a) and (b) were included in all groups, and 6 additional

* Corresponding author at: School of Engineering, University of Western Sydney, Penrith South DC, NSW 1797, Australia. Tel.: +61 2 4736 0064; fax: +61 2 4736 0054.
E-mail addresses: z.tao@uws.edu.au, taozhong@fzu.edu.cn (Z. Tao).

0143-974X/$ – see front matter © 2010 Elsevier Ltd. All rights reserved.
doi:10.1016/j.jcsr.2010.10.004

Nomenclature

A_c	Cross-sectional area of concrete
A_s	Cross-sectional area of steel
B	Width of the square or rectangular steel tube
D	Diameter of the circular steel tube
E	Load eccentricity
E_0	Initial elastic modulus of stainless steel
E_s	Carbon steel modulus of elasticity
f_c'	Compressive cylinder strength of concrete
f_{ck}	Characteristic concrete strength ($=0.67f_{cu}$)
f_{cu}	Compressive cube strength of concrete
f_y	Yield strength of carbon steel
H	Overall depth of the rectangular steel tube
L	Specimen length
L_e	Effective length
M	Bending moment
n	Strain-hardening exponent
N	Axial load
$N_{\max}$	Maximum load
N_{uc}	Predicted strength
N_{ue}	Ultimate strength
t	Wall thickness of the steel tube
u_m	Mid-height deflection of a slender column
$u_{m,\mathrm{ult}}$	Mid-height deflection of a slender column at its peak load
α	Steel ratio ($=A_s/A_c$)
Δ	Axial shortening
ε	Strain
ε_{cu}	Axial strain at extreme compression fibre corresponding to N_{ue}
ε_L	Lateral strain at extreme compression fibre corresponding to N_{ue}
$\varepsilon_{\max}$	Axial strain corresponding to $N_{\max}$
λ	Slenderness ratio
μ	Average value
ν	Lateral-to-axial strain ratio
σ	Standard deviation
$\sigma_{0.2}$	0.2% proof stress of stainless steel
ξ	Confinement factor $\left(=\frac{A_s \cdot f_y}{A_c \cdot f_{ck}}\right)$

rectangular specimens with a cross-section shown in Fig. 1(c) were investigated in the last group. The three kinds of sections are the most popular ones used in engineering practice. After researching the available products on the market, the overall depth of the rectangular columns was chosen to be about two times their width (B). For short columns included in groups I–III, the height (L) of them was chosen to be about three times the diameter (D) of the circular sections or the width (B) of the square sections. This was to ensure that the test results could be used to evaluate the cross-sectional performance of CFSST columns [11]. More details of the specimens are provided in Tables 1–4, respectively.

2.2. Material properties

Type 304 austenitic stainless steel according to Australian/New Zealand Standard AS/NZS 4673: 2001 [12] was used to fabricate the specimens. A series of coupon tests were conducted to determine the material properties of the stainless steel, where the tensile coupons for square or rectangular steel tubes were taken from the flat surfaces of each tube size. The material test results indicate that the stainless steel showed obvious non-linear stress–strain characteristics, as shown in Fig. 2. The three basic Ramberg–Osgood parameters, i.e., the initial elastic modulus E_0, the 0.2% proof stress $\sigma_{0.2}$, and the strain-hardening exponent n, for all types of tubes used are presented in Tables 1–3 and 5, respectively.

Since the corner effect is usually expected to be very pronounced for stainless steel material [13], tensile corner coupons were also prepared to measure the material properties in the corner regions of the square and rectangular tubes used for the specimens included in Group IV. The internal radii of rounded corners were 1.8 mm and 0.8 mm for the square and rectangular tubes, respectively. In preparing a corner coupon, it included the corner radius and a distance of $2t$ extending to each flat region according to Ashraf et al. [13], where t is the tube thickness. The measured 0.2% proof stress $\sigma_{0.2}$, ultimate strength and elongation after fracture are 562.4 MPa, 902.7 MPa and 37.2%, respectively, for the corner material of the square tubes; whilst those for the corner material of the rectangular tubes are 669.2 MPa, 967.4 MPa and 36.6%, respectively. The cold-worked corner regions of the square and rectangular tubes have 0.2% proof strengths 44.1% and 84.2% higher than the 0.2% proof strengths of the flat regions, respectively. A corresponding loss in ductility is also accompanied, as shown in Fig. 2(a).

Apart from the above steel coupon tests, three compressive tests on steel hollow sections were also conducted for each type of tubes presented in Table 5 to compare the behaviour of stainless steel in compression. The length of these stub columns was chosen to be three times the major cross-sectional dimension. The measured average peak loads (N_p) for different tube shapes are given in Table 5. In general, the obtained axial stress (σ)-axial strain (ε) curve in compression coincides with the curve in tension before the peak load of a stub column was reached. Due to the local buckling effect, the σ–ε curves obtained from the stub column tests, however, experienced significant strain-softening. One of the test results of square stub columns is selected to illustrate this phenomenon, as shown in Fig. 2(b).

Concrete cylinders were cast and tested to determine the compressive strength (f_c') of the concrete. The average compressive strengths at the time of testing for the columns in each series are given in Tables 1–4, respectively. It should be noted that only average concrete strength at 28 days of 51.6 MPa was available for the composite specimens presented in Table 2. Owing to an equipment malfunction, those specimens were not tested until nine months after the 28 days compressive strength tests were carried out. Therefore, a formula recommended in [14] was used to predict the concrete strength at the time of tests, and a predicted value of 62.4 MPa was obtained.

2.3. Specimen preparation

Cold-formed hollow stainless steel sections were cut according to their required dimensions. Measurements were carried out with an aim to obtain global geometric imperfections for these slender columns using a stretching metal wire and a Vernier caliper. It appears from the results that these tubes were almost ideally straight, and no visible imperfections could be measured.

Commercial concrete was ordered and delivered to the laboratory. The concrete was filled in layers and a vibrator was used for compaction requirements except when preparing the six composite columns presented in Table 3. The concrete of these columns was compacted by a wooden stick instead. It is expected that this compaction method had a minor influence on the performance of short columns according to Han [15].

2.4. Instrumentation and test setup

Short specimens under axial compression were placed into the testing machine and the loads were applied on the specimens directly, as shown in Fig. 3(a). For short specimens under combined

Table 1
Test data of short columns under axial compression (Group I).

No.	Specimen label	$D \times t \times L$ (mm)	D/t	E_0 (MPa)	$\sigma_{0.2}$ (MPa)	n	f_c' (MPa)	N_{max} (kN)	ε_{max}	N_{ue} (kN)	ε_{cu} ($\mu\varepsilon$)	Curve type
1	CH-50x1.2A	50.8 × 1.2 × 150	42.3	195 000	291	7	–	86	0.021	80	10 000	C
2	CH-50x1.2B	50.8 × 1.2 × 150	42.3	195 000	291	7	–	83	0.026	71	10 000	C
3	C20-50x1.2A	50.8 × 1.2 × 150	42.3	195 000	291	7	20	192*	0.178	106	10 000	A
4	C20-50x1.2B	50.8 × 1.2 × 150	42.3	195 000	291	7	20	164*	0.149	112	10 000	A
5	C30-50x1.2A	50.8 × 1.2 × 150	42.3	195 000	291	7	30	225*	0.160	134	10 000	A
6	C30-50x1.2B	50.8 × 1.2 × 150	42.3	195 000	291	7	30	237*	0.145	130	10 000	A
7	CH-50x1.6A	50.8 × 1.6 × 150	31.8	195 000	298	7	–	104	0.032	92	10 000	C
8	CH-50x1.6B	50.8 × 1.6 × 150	31.8	195 000	298	7	–	105	0.030	93	10 000	C
9	C20-50x1.6A	50.8 × 1.6 × 150	31.8	195 000	298	7	20	203*	0.139	132	10 000	A
10	C20-50x1.6B	50.8 × 1.6 × 150	31.8	195 000	298	7	20	222*	0.138	140	10 000	A
11	C30-50x1.6A	50.8 × 1.6 × 150	31.8	195 000	298	7	30	260*	0.177	167	10 000	A
12	C30-50x1.6B	50.8 × 1.6 × 150	31.8	195 000	298	7	30	280*	0.179	162	10 000	A
13	CH-100x1.6A	101.6 × 1.6 × 300	63.5	195 000	320	7	–	178	0.011	176	10 000	C
14	CH-100x1.6B	101.6 × 1.6 × 300	63.5	195 000	320	7	–	175	0.012	170	10 000	C
15	C20-100x1.6A	101.6 × 1.6 × 300	63.5	195 000	320	7	20	637*	0.191	421	10 000	A
16	C20-100x1.6B	101.6 × 1.6 × 300	63.5	195 000	320	7	20	675*	0.206	426	10 000	A
17	C30-100x1.6A	101.6 × 1.6 × 300	63.5	195 000	320	7	30	602*	0.154	477	10 000	B
18	C30-100x1.6B	101.6 × 1.6 × 300	63.5	195 000	320	7	30	609*	0.163	477	10 000	B
19	CH-127x1.6A	127 × 1.6 × 400	79.4	195 000	274	7	–	254	0.0062	254	6 175	C
20	CH-127x1.6B	127 × 1.6 × 400	79.4	195 000	274	7	–	267	0.0093	267	9 275	C
21	C20-127x1.6A	127 × 1.6 × 400	79.4	195 000	274	7	20	789*	0.109	664	10 000	B
22	C20-127x1.6B	127 × 1.6 × 400	79.4	195 000	274	7	20	809*	0.116	685	10 000	B
23	C30-127x1.6A	127 × 1.6 × 400	79.4	195 000	274	7	30	815*	0.115	743	10 000	B
24	C30-127x1.6B	127 × 1.6 × 400	79.4	195 000	274	7	30	790*	0.139	748	10 000	B
25	CH-150 x1.6A	152.4 × 1.6 × 450	95.3	195 000	279	7	–	240	0.0058	240	5 822	C
26	CH-150 x1.6B	152.4 × 1.6 × 450	95.3	195 000	279	7	–	240	0.0068	240	6 822	C
27	C20-150x1.6A	152.4 × 1.6 × 450	95.3	195 000	279	7	20	897*	0.127	816	10 000	B
28	C20-150x1.6B	152.4 × 1.6 × 450	95.3	195 000	279	7	20	941*	0.136	801	10 000	B
29	C30-150x1.6A	152.4 × 1.6 × 450	95.3	195 000	279	7	30	997*	0.133	904	10 000	B
30	C30-150x1.6B	152.4 × 1.6 × 450	95.3	195 000	279	7	30	952*	0.130	890	10 000	B
31	CH-200x2.0A	203.2 × 2.0 × 500	101.6	195 000	259	7	–	367	0.0055	367	5 467	C
32	CH-200x2.0B	203.2 × 2.0 × 500	101.6	195 000	259	7	–	362	0.0055	362	5 483	C
33	C20-200x2.0A	203.2 × 2.0 × 500	101.6	195 000	259	7	20	1406*	0.104	1390	7 833	B
34	C20-200x2.0B	203.2 × 2.0 × 500	101.6	195 000	259	7	20	1397*	0.096	1378	8 283	B
35	C30-200x2.0A	203.2 × 2.0 × 500	101.6	195 000	259	7	30	1537*	0.101	1522	8 617	B
36	C30-200x2.0B	203.2 × 2.0 × 500	101.6	195 000	259	7	30	1550*	0.107	1550	9 234	B
37	SH-50x2A	51 × 1.81 × 150	28.2	205 100	353	10.4	–	184	0.0078	184	7 825	C
38	SH-50x2B	51 × 1.81 × 150	28.2	205 100	353	10.4	–	180	0.0068	180	6 838	C
39	S20-50x2A	51 × 1.81 × 150	28.2	205 100	353	10.4	21.5	261	0.066	234	10 000	A
40	S20-50x2B	51 × 1.81 × 150	28.2	205 100	353	10.4	21.5	256	0.064	243	10 000	A
41	S30-50x2A	51 × 1.81 × 150	28.2	205 100	353	10.4	34.9	282*	0.095	268	9 483	B
42	S30-50x2B	51 × 1.81 × 150	28.2	205 100	353	10.4	34.9	278	0.065	274	10 000	B
43	SH-50x3A	51 × 2.85 × 150	17.9	207 900	440	8.2	–	319	0.027	293	10 000	C
44	SH-50x3B	51 × 2.85 × 150	17.9	207 900	440	8.2	–	315	0.020	302	10 000	C
45	S20-50x3A	51 × 2.85 × 150	17.9	207 900	440	8.2	21.5	399*	0.119	358	10 000	B
46	S20-50x3B	51 × 2.85 × 150	17.9	207 900	440	8.2	21.5	417*	0.099	364	10 000	A
47	S30-50x3A	51 × 2.85 × 150	17.9	207 900	440	8.2	34.9	543*	0.202	394	10 000	A
48	S30-50x3B	51 × 2.85 × 150	17.9	207 900	440	8.2	34.9	460*	0.170	393	10 000	A
49	SH-100x3A	100 × 2.85 × 300	35.1	195 700	358	8.3	–	448	0.0062	448	6 217	C
50	SH-100x3B	100 × 2.85 × 300	35.1	195 700	358	8.3	–	457	0.0045	457	4 478	C
51	S20-100x3A	100 × 2.85 × 300	35.1	195 700	358	8.3	21.5	705	0.0084	705	8 420	C
52	S20-100x3B	100 × 2.85 × 300	35.1	195 700	358	8.3	21.5	716	0.0054	716	5 397	C
53	S30-100x3A	100 × 2.85 × 300	35.1	195 700	358	8.3	34.9	765	0.0047	765	4 653	C
54	S30-100x3B	100 × 2.85 × 300	35.1	195 700	358	8.3	34.9	757	0.057	742	4 592	C
55	SH-100x5A	101 × 5.05 × 300	20.0	202 100	435	7.0	–	1185	0.024	1036	10 000	C
56	SH-100x5B	101 × 5.05 × 300	20.0	202 100	435	7.0	–	1241	0.020	1154	10 000	C
57	S20-100x5A	101 × 5.05 × 300	20.0	202 100	435	7.0	21.5	1437	0.029	1352	10 000	A
58	S20-100x5B	101 × 5.05 × 300	20.0	202 100	435	7.0	21.5	1449	0.029	1348	10 000	A
59	S30-100x5A	101 × 5.05 × 300	20.0	202 100	435	7.0	34.9	1474	0.054	1434	10 000	A
60	S30-100x5B	101 × 5.05 × 300	20.0	202 100	435	7.0	34.9	1490	0.027	1461	10 000	A
61	SH-150x3A	152 × 2.85 × 450	53.3	192 600	268	6.8	–	372	0.0019	372	1 931	C
62	SH-150x3B	152 × 2.85 × 450	53.3	192 600	268	6.8	–	366	0.0026	366	2 568	C
63	S20-150x3A	152 × 2.85 × 450	53.3	192 600	268	6.8	21.5	1035	0.0042	1035	4 238	C
64	S20-150x3B	152 × 2.85 × 450	53.3	192 600	268	6.8	21.5	1062	0.0024	1062	2 446	C
65	S30-150x3A	152 × 2.85 × 450	53.3	192 600	268	6.8	34.9	1074	0.0015	1074	1 545	C
66	S30-150x3B	152 × 2.85 × 450	53.3	192 600	268	6.8	34.9	1209	0.0029	1209	2 883	C
67	SH-150x5A	150 × 4.80 × 450	31.3	192 200	340	5.6	–	1181	0.0053	1181	5 274	C
68	SH-150x5B	150 × 4.80 × 450	31.3	192 200	340	5.6	–	1183	0.0043	1183	4 294	C
69	S20-150x5A	150 × 4.80 × 450	31.3	192 200	340	5.6	21.5	1844	0.107	1804	6 965	C
70	S20-150x5B	150 × 4.80 × 450	31.3	192 200	340	5.6	21.5	1935	0.100	1798	9 832	C
71	S30-150x5A	150 × 4.80 × 450	31.3	192 200	340	5.6	34.9	2048*	0.066	1947	5 634	C
72	S30-150x5B	150 × 4.80 × 450	31.3	192 200	340	5.6	34.9	1976	0.0060	1976	6 036	C

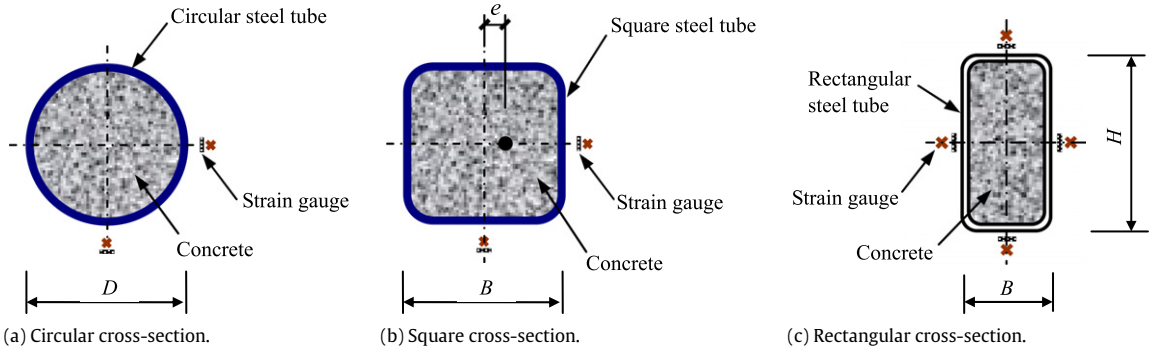

(a) Circular cross-section. (b) Square cross-section. (c) Rectangular cross-section.

Fig. 1. Cross-sections of CFSST columns.

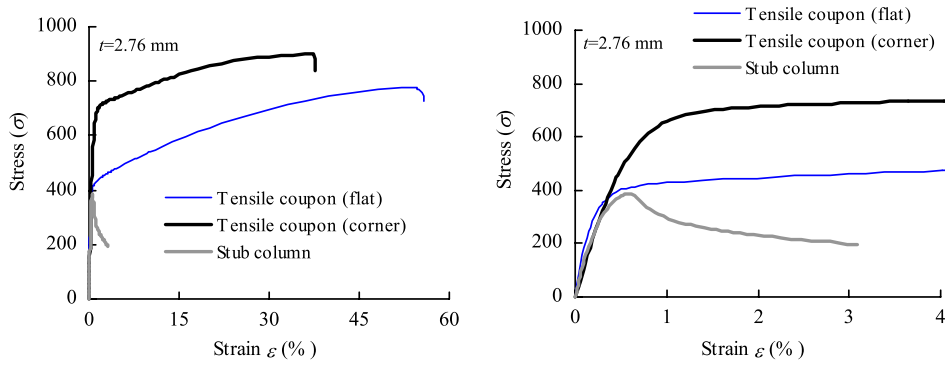

(a) Full curves. (b) Initial curves.

Fig. 2. Typical measured stress–strain curves for stainless steel (square cross-section).

Table 2
Test data of short columns under different loading methods (Group II).

Section type	No.	Specimen label	$D(B) \times t \times L$ (mm)	$D(B)/t$	E_0 (MPa)	$\sigma_{0.2}$ (MPa)	n	f_c' (MPa)	N_{max} (kN)	ε_{max} ($\mu\varepsilon$)
Circular	1	H1-127	127 × 1.6 × 375	79.4	195 000	274	7	–	259	5940
	2	S1-127	127 × 1.6 × 375	79.4	195 000	274	7	62.4	284	4997
	3	CFT1-127	127 × 1.6 × 375	79.4	195 000	274	7	62.4	1288	3983
	4	H2-152	152.4 × 1.6 × 450	95.3	195 000	279	7	–	241	4266
	5	S2-152	152.4 × 1.6 × 450	95.3	195 000	279	7	62.4	263	6374
	6	CFT2-152	152.4 × 1.6 × 450	95.3	195 000	279	7	62.4	1744	2487
Square	7	H3-150	150 × 4.8 × 450	31.3	192 200	340	5.6	–	1179	4486
	8	S3-150	150 × 4.8 × 450	31.3	192 200	340	5.6	62.4	1315	6421
	9	CFT3-150	150 × 4.8 × 450	31.3	192 200	340	5.6	62.4	2546	2455

Table 3
Test data of square columns under combined actions (Group III).

No.	Specimen label	$B \times t \times L$ (mm)	B/t	E_0 (MPa)	$\sigma_{0.2}$ (MPa)	n	f_c' (MPa)	e (mm)	N_{max} (kN)
1	H-3-0	101 × 2.85 × 300	35.1	195 700	358	8.3	–	0	447
2	C-3-0	101 × 2.85 × 300	35.1	195 700	358	8.3	12	0	721
3	H-3-20	101 × 2.85 × 300	35.1	195 700	358	8.3	–	20	340
4	C-3-20	101 × 2.85 × 300	35.1	195 700	358	8.3	12	20	512
5	H-3-40	101 × 2.85 × 300	35.1	195 700	358	8.3	–	40	247
6	C-3-40	101 × 2.85 × 300	35.1	195 700	358	8.3	12	40	389
7	H-5-0	101 × 5.05 × 300	20.0	202 100	435	7.0	–	0	1185
8	C-5-0	101 × 5.05 × 300	20.0	202 100	435	7.0	12	0	1447
9	H-5-20	101 × 5.05 × 300	20.0	202 100	435	7.0	–	20	833
10	C-5-20	101 × 5.05 × 300	20.0	202 100	435	7.0	12	20	1043
11	H-5-40	101 × 5.05 × 300	20.0	202 100	435	7.0	–	40	625
12	C-5-40	101 × 5.05 × 300	20.0	202 100	435	7.0	12	40	752

actions, sharp knife edges were designed and attached to the 30 mm thick end plates of the specimens (Fig. 3(b)). Two 6 mm deep grooves of 20 and 40 mm from the centre were machined into the plates to apply moments with different eccentricities (e). As far as the specimens in Group IV are concerned, two semi-spherical hinges with a height of 70 mm were installed at both ends of each column before testing to simulate pin-ended supports, as shown in Fig. 14(b). No intended load eccentricity was enforced for the specimens. Therefore, the effective length (L_e) of a specimen shown in Table 4 was taken as its physical length (L) plus 140 mm.

A total of six strain gauges were attached to two sides of each short column as shown in Fig. 1(a) and (b), in which two

Table 4
Test data of slender columns under axial compression (Group IV).

Section type	No.	Specimen label	$D(B)$ (mm)	H (mm)	t	L_e (mm)	λ	$\sigma_{0.2}$ (MPa)	f_c' (MPa)	N_{ue} (kN)	$u_{m,ult}$ (mm)	ε_{cu} ($\mu\varepsilon$)	ε_L ($\mu\varepsilon$)
Circular	1	C1-1a	113.6	–	2.8	485	17.1	288.6	36.3	738.0	0.39	−19 297	13 402
	2	C1-1b	113.6	–	2.8	485	17.1	288.6	75.4	1137.1	0.24	−7 819	5 349
	3	C1-2a	113.6	–	2.8	1540	54.2	288.6	36.3	578.9	2.07	−5 443	3 278
	4	C1-2b	113.6	–	2.8	1540	54.2	288.6	75.4	851.1	2.58	−3 197	1 304
	5	C1-3a	113.6	–	2.8	2940	103.5	288.6	36.3	357.6	11.80	−1 630	479
	6	C1-3b	113.6	–	2.8	2940	103.5	288.6	75.4	731.8	3.65	−2 014	646
	7	C2-1a	101	–	1.48	440	17.4	320.6	36.3	501.3	1.28	−10 205	8 191
	8	C2-1b	101	–	1.48	440	17.4	320.6	75.4	819.0	0.28	−5 339	3 530
	9	C2-2a	101	–	1.48	1340	53.1	320.6	36.3	446.0	1.70	−3 653	2 100
	10	C2-2b	101	–	1.48	1340	53.1	320.6	75.4	692.9	1.94	−3 048	1 256
	11	C2-3a	101	–	1.48	2540	100.6	320.6	36.3	383.0	1.25	−1 813	626
	12	C2-3b	101	–	1.48	2540	100.6	320.6	75.4	389.7	13.69	−2 462	840
Square	13	S1-1a	100.3	–	2.76	440	15.2	390.3	36.3	767.6	0.33	−9 102	5 778
	14	S1-1b	100.3	–	2.76	440	15.2	390.3	75.4	1090.5	0.29	−3 846	2 162
	15	S1-2a	100.3	–	2.76	1340	46.3	390.3	36.3	697.3	2.65	−4 383	2 465
	16	S1-2b	100.3	–	2.76	1340	46.3	390.3	75.4	1022.9	0.83	−3 040	1 557
	17	S1-3a	100.3	–	2.76	2540	87.7	390.3	36.3	622.9	4.42	−2 451	1 773
	18	S1-3b	100.3	–	2.76	2540	87.7	390.3	75.4	684.2	10.82	−2 423	1 050
Rectangular	19	R1-1a	49	99.5	1.93	440	31.1	363.3	36.3	385.6	0.63	−6 379	2 682
	20	R1-1b	49	99.5	1.93	440	31.1	363.3	75.4	558.3	0.15	−5 086	1 400
	21	R1-2a	49	99.5	1.93	740	52.3	363.3	36.3	361.1	1.70	−6 758	–
	22	R1-2b	49	99.5	1.93	740	52.3	363.3	75.4	517.7	0.47	−3 522	1 856
	23	R1-3a	49	99.5	1.93	1340	94.7	363.3	36.3	262.8	6.48	−2 101	1 069
	24	R1-3b	49	99.5	1.93	1340	94.7	363.3	75.4	332.8	11.89	−3 571	1 855

Table 5
Material properties of stainless steel used for specimens in Group IV.

Steel thickness (mm)	Initial elastic modulus E_0 (GPa)	0.2% proof stress $\sigma_{0.2}$ (MPa)	Strain-hardening exponent n	Poisson's ratio	Yield strain (10^{-6})	Ultimate strength (MPa)	Elongation percentage (%)	N_p (kN)
2.8	173.9	288.6	7.6	0.262	3648	689.5	74.5	326.0
1.48	184.2	320.6	7.2	0.293	3740	708.0	54.9	159.6
2.76	182.0	390.3	6.7	0.291	4145	762.1	54.3	419.2
1.93	195.3	363.3	6.1	0.285	3860	751.6	58.0	195.1

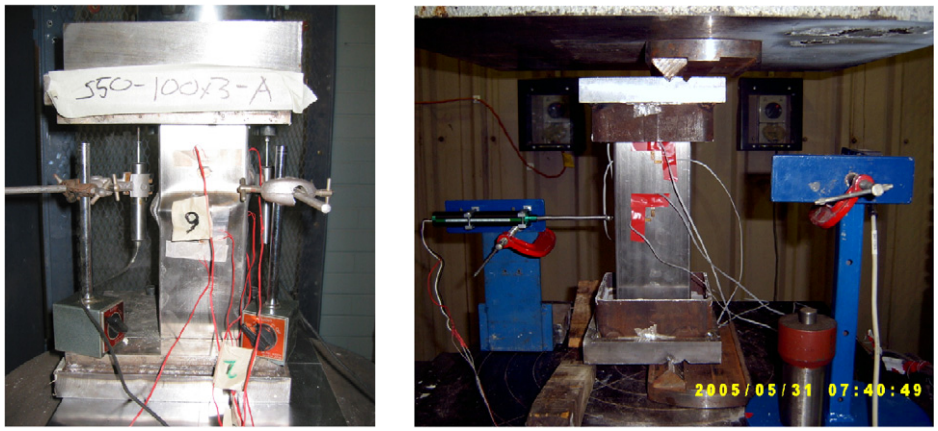

(a) Specimen under axial compression. (b) Specimen under axial compression combined with bending.

Fig. 3. Test setup for short columns under axial compression and combined actions.

axial and two transverse strain gauges were attached at the mid-height, whilst only two axial strain gauges were used at the quarter-height. In addition to the strain gauges, one or two linear variable displacement transducers (LVDT) were used to measure the specimen shortening (Fig. 3(a)). For those short columns under combined actions, a Midory LVDT at the mid-height was used to measure the lateral deflection, as shown in Fig. 3(b). Six LVDTs were used to measure the out-of-plane deflections of a column in Group IV at two perpendicular directions along the specimen height. Owing to the limited installation space, deflections were only measured at the mid-height for those short specimens with a L_e below 500 mm. Eight strain gauges with a gauge length of 3 mm were used for each specimen to measure the longitudinal and transverse strains at the mid-height, as shown in Fig. 1(c).

3. Experimental results and discussion

3.1. Axial load behaviour of stub columns

Twenty four circular CFST stub columns and 12 circular hollow tubes with details shown in Table 1 were tested. Different specimen designations were used to distinguish the specimens,

(a) Circular CFST. (b) Circular hollow tube. (c) Square CFST. (d) Square hollow tube.

Fig. 4. Failure modes of CFST stub columns and hollow tubes.

where the letters CH denote hollow tubes; C20 and C30 denote CFST columns with a concrete strength of 20 MPa and 30 MPa, respectively. The following numbers in the specimen labels represent the nominal diameter and thickness of the tubes. At the same time, two identical specimens were designed to ensure that the experimental results were reliable, where an affixed letter A or B was included in the labels. A similar test program and specimen designation system was used for those square CFST stub columns and hollow tubes, as shown in Table 1, where S20 and S30 in the labels denote square CFST columns and SH represents square hollow tubes.

The parameters considered in this study are: (1) section types, circular and square; (2) cross-section slenderness D/t or B/t, from 18 to 102; (3) filling the hollow sections with concrete or not; and (4) concrete cylinder strength f_c', from 20 to 35 MPa.

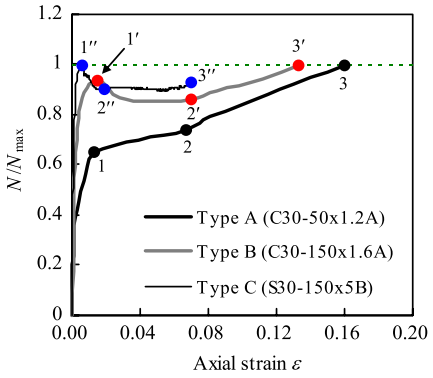

Fig. 5. Typical axial load (N) versus axial strain (ε) curves for stub columns.

3.1.1. Failure modes

The failure mode for both circular and square CFSST columns was a local (outward folding) failure mechanism as shown in Fig. 4(a) and (c). For a typical empty circular hollow section (CHS) with a D/t ratio of 79.4 or beyond, it formed "elephant foot" buckling as shown in Fig. 4(b). Other thicker empty CHS sections normally locally buckled near the mid-height. The empty square hollow sections (SHS) experienced local failure mechanism where the steel plates buckled alternately in convex and concave surfaces, shown in Fig. 4(d). Compared with conventional carbon steel CFST columns or hollow tubes, it seems that there is no obvious difference in terms of test observations and failure modes. However, the amplitudes of the local buckles for the stainless steel tubes are much higher, and the overall axial shortening for some specimens can be as high as 20% without the observation of possible fracture of the stainless steel tubes. This is attributed to the fact that the stainless steel material shows much higher ductility than carbon steel [16].

3.1.2. Test results and discussion

The maximum loads (N_{max}) recorded in the tests and the corresponding axial strains (ε_{max}) are summarised in Table 1. It should be noted that, for all of the 24 circular CFST columns and 6 square CFST columns, these tests stopped owing to the apparent over-deformation as shown in Fig. 4, and the maximum loads were obtained at the end of the testing. It seems that there was still potential to achieve higher load-carrying capacity for these specimens. In order to distinguish these specimens from the others, N_{max} of them presented in Table 1 are marked with stars.

To analyse the behaviour of CFSST stub columns, test curves of axial load (N) versus axial strain (ε) are compared as follows. The axial strains were measured from strain gauges and LVDT(s), where the strain gauge measurements were only used before the occurrence of tube buckling, and after that the axial shortening measured by the LVDT(s) was used to evaluate the post-buckling behaviour of a test specimen [17].

Generally, the N–ε curves obtained can be classified into three types, as shown in Fig. 5, which depend mainly on the confinement of steel tubes to concrete. The N–ε relationship changes from Type A to Type B and then to Type C as the confinement decreases, with three typical curves shown in Fig. 5. The corresponding curve types for other specimens are given in Table 1.

Type A is the typical N–ε relationship with a strain-hardening response. Ten circular CFST stub columns and nine square CFST stub columns have curves that can be classified into Type A group. These types of curves have an initial linear portion followed by a transitional and plastic portion. After reaching Point 1, there is a portion with small slope until reaching Point 2. If the confinement is not effective enough, this portion can be a nearly horizontal flat one. The bigger the cross-section slenderness, the larger the strain at Point 2 and the smaller the slope is. The nonlinear response at this stage is from the yielding and local buckling of the steel tubes and the nonlinear behaviour of the confined concrete. Thereafter, the curve is almost linear with an

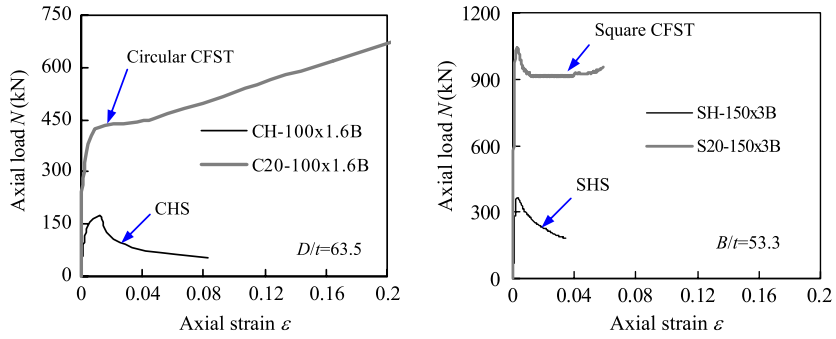

(a) Circular stub column. (b) Square stub column.

Fig. 6. Effect of concrete filling on $N-\varepsilon$ curves.

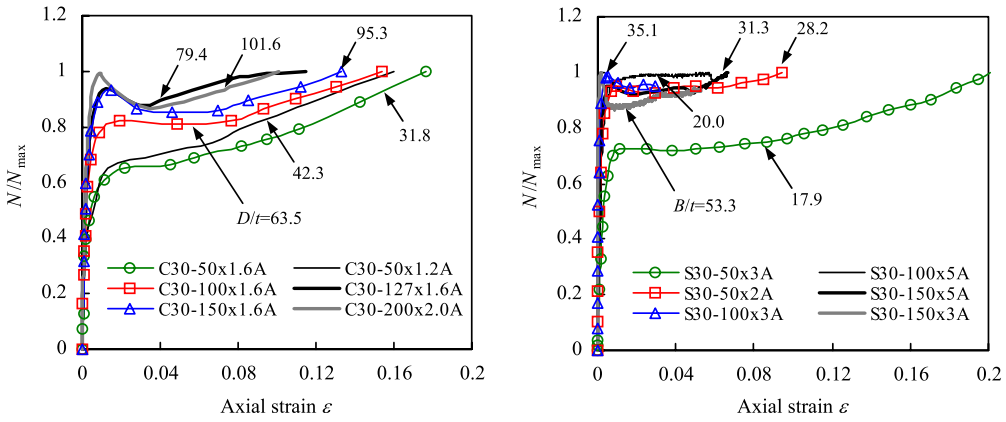

(a) Circular stub column. (b) Square stub column.

Fig. 7. Effect of cross-section slenderness on $N-\varepsilon$ curves.

increased slope, and the load keeps increasing until the end of the test (Point 3). This is attributed to the fact that stainless steel shows very high strain hardening and has extremely good deformation capacity. Therefore, the steel tube can exert high confinement on the concrete core after undergoing substantial plastic deformation.

Compared with Type A, Type B curves show similar features except the existence of the declining portion 1′2′. Most circular CFST stub columns with larger D/t ratios and three square CFST stub columns have $N-\varepsilon$ relationship that can be classified into Type B group. After reaching the first peak Point 1′ and without sufficient tube confinement, the load of a column with Type B curve decreases with increasing axial deformation until reaching Point 2′. After that, the load increases once again to Point 3′ at the end of the test due to the strain hardening effect of stainless steel. From the test observation, it seems that the corresponding load at Point 3′ is generally bigger than that at Point 1′.

Type C is the typical $N-\varepsilon$ relationship with a strain-softening response which is very common for conventional carbon steel CFST stub columns. In the current tests, the Type C curves were observed only for half of the square CFST stub columns owing to the less tube confinement on concrete. No circular CFST stub column in the tests had Type C $N-\varepsilon$ curve. For a Type C curve, the load decreases with an increase of axial deformation after reaching the peak load (Point 1″), and remains almost steady beyond Point 2″. Generally, the residual strength is much higher compared with that of a conventional carbon steel CFST column with same parameters.

Owing to the influence of local buckling, all hollow sections showed the pattern of Type C curves. This is not surprising since there was no in-fill concrete to restrain the tube buckling. The smaller the cross-section slenderness, the higher the deformation capacity and compressive strength were.

Fig. 6 demonstrates the effect of concrete filling on the $N-\varepsilon$ curves. As can be seen, the modulus and strength are greatly enhanced for both the circular and square columns when concrete is filled in the hollow sections. This comparison shows that a filled section has a much higher deformation capacity than its empty counterpart, and shows more ductile behaviour especially when the tube shape is circular. Obviously, the concrete filling is very beneficial to exert the material's behaviour and make the best use of stainless steel.

The effects of cross-section slenderness on the $N-\varepsilon$ curves for circular and square stub columns are demonstrated in Fig. 7(a) and (b). The stub columns with larger D/t or B/t ratio are generally less ductile, since a steel tube with a smaller D/t or B/t ratio is more effective to exert confinement on concrete. This can be proved by the measured lateral strains of steel tubes in the current tests. This trend is the same as that observed by many other researchers when conducting tests on conventional carbon steel CFST columns [3,17].

Since the range of concrete strength varied for the specimens in Group I was not very wide, it seems that the concrete's strength has no significant effect on the shape of $N-\varepsilon$ curves, though the column strength increases with increasing concrete strength. Nevertheless, there is still a trend that hollow sections filled with higher strength concrete are less ductile.

To evaluate the possible behaviour differences between stainless steel and carbon steel CFST columns, the $N-\varepsilon$ curves of CFSST columns obtained from the current tests are compared with those carbon steel ones available in the literature. To make a meaningful comparison, particular care should be taken to choose the test specimens, which is described in the following.

A confinement factor (ξ) was presented by Han et al. [18,19] to address the passive confinement of carbon steel tube on concrete.

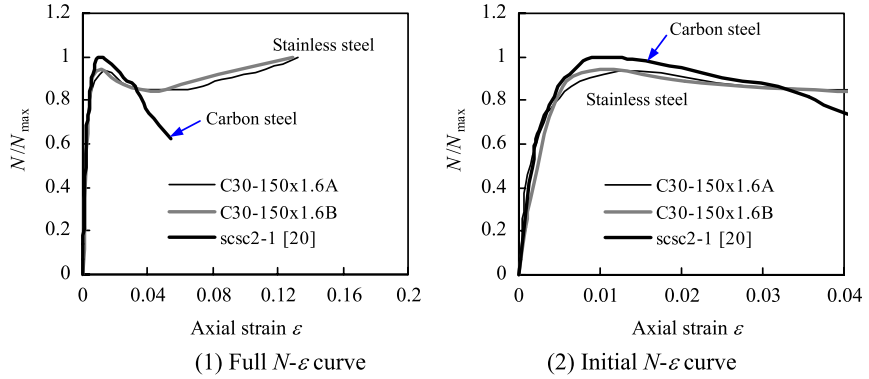

(a) Circular section.

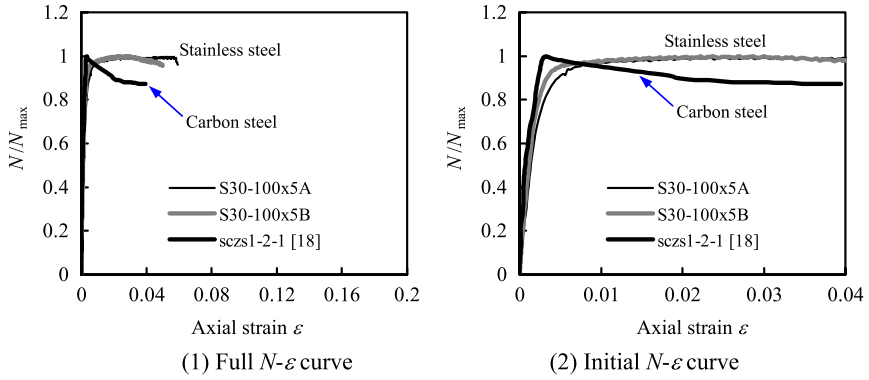

(b) Square section.

Fig. 8. Comparison of N–ε curves between stainless steel and carbon steel CFST stub columns.

The expression of ξ is as follows:

$$\xi = \frac{A_s \cdot f_y}{A_c \cdot f_{ck}} = \alpha \cdot \frac{f_y}{f_{ck}} \tag{1}$$

where A_s and A_c are the cross-sectional areas of the steel and concrete, respectively; α ($=A_s/A_c$) is the steel ratio; f_y is the yield strength of the carbon steel; and f_{ck} is the characteristic strength of the concrete. The value of f_{ck} is determined using 67% of the compressive strength of cubic blocks (f_{cu}) for normal strength concrete. It was found that the higher the ξ, the more ductile the confined concrete is. Therefore, the ξ, to some extent, represents the composite action between steel tubes and concrete [18,19].

Therefore, the confinement factor (ξ) is chosen herein to make sure the selected carbon steel and corresponding CFSST specimens have very close ξ. For circular columns, the carbon steel specimen scsc2-1 presented by Han and Yao [20] is compared with the current test specimens C30-150x1.6A and C30-150x1.6B. All of them have a same ξ of 0.49. The carbon steel specimen sczs1-2-1 with an ξ of 3.52 presented in [18] is compared with specimens S30-100x5A and S30-100x5B with an ξ of 3.59 in Table 1. Since no cube strength of concrete was measured in this test program, the equivalent cube strength was determined using the reported cylinder strength. This was based on the relationship of two types of concrete strengths presented by Chen et al. [21], and reflected in a table presented in [22]. The 0.2% proof stress $\sigma_{0.2}$ for stainless steel is used to replace f_y in Eq. (1) to calculate ξ. The parameters for the circular specimen scsc2-1 are: $D \times t = 200 \times 3$ mm, $f_y = 303.5$ MPa, $f_{cu} = 58.5$ MPa, steel modulus of elasticity $E_s = 206\,500$ MPa, $N_{max} = 2320$ kN; whilst those for the square specimen sczs1-2-1 are: $B \times t = 140 \times 3.84$ mm, $f_y = 330$ MPa, $f_{ck} = 10.65$ MPa, $E_s = 200\,000$ MPa, $N_{max} = 941$ kN.

Fig. 8 shows that the shape of the N–ε curve for a CFSST column is quite different from that of a carbon steel CFST column with a close confinement factor ξ. The CFSST column shows more gradual yielding behaviour owing to the fact that the nonlinear stress–strain curve of stainless steel is of the "roundhouse" type [16]. More obviously, a CFSST column has much higher residual strength even after experienced large axial deformation compared with its carbon steel counterpart. This feature of CFSST columns makes them very favourable to be used as structural columns that are most likely to be subjected to extreme loads, like explosion, collision and fire exposure.

3.2. Influence of loading methods

Six circular and three square stub columns as shown in Table 2, were tested under axial compression to evaluate the influence of different loading methods. Three tubes with different shapes or sizes were designed, consisting of two circular sections and one square section. For each type of cross-section, three different stainless steel specimens were included as follows:

(1) One hollow section with an H in the specimen label, as shown in Table 2, to observe its axial loading behaviour.
(2) One hollow section filled with concrete, leaving approximately 20–25 mm clearance below the top and above the bottom of the steel tube (denoted as 'S' in Table 2). In this case, only the steel tube was loaded, and the concrete was expected to restrict the steel casing from buckling inwards. To avoid possible tube local buckling occurred at the ends where the concrete was recessed, four external stiffeners were welded on each tube end, as shown in Fig. 9.
(3) One CFST column with concrete flush with the top and bottom of the specimen. This column is denoted as 'CFT' in Table 2, and both the concrete and steel were loaded simultaneously during the testing.

(a) Circular section.

(b) Square section.

Fig. 9. Failure modes of stub columns under different loading conditions.

Fig. 9 compares the failure modes of the stub columns under different loading methods. The failure modes for the empty tubes and CFST columns are virtually the same as those described in the above Section 3.1.1. For the specimens with concrete restriction in the S series where only the steel tubes were loaded, they experienced outward buckling right around the specimen at which local buckling occurred. This phenomenon is the same as that observed in the CFST columns. The former, however, only formed apparent local buckling at a location near one specimen end as shown in Fig. 9, whilst buckling occurred at different locations along the column's height for the CFST columns.

The maximum loads (N_{max}) recorded in the tests are presented in Table 2. Owing to the concrete's contribution in carrying axial load, a CFST composite column has a much higher load-carrying capacity than the corresponding specimen in the H or S series. It is worth noting that a specimen in the S series has a slightly higher N_{max} compared with the corresponding empty tube. The strength increases for the circular specimens S1-127 and S2-152 are 9.65% and 9.13%, respectively, whilst the increase for the square specimen S3-150 is 11.54%.

O'Shea and Bridge [23,24] conducted axial compression tests on thin-walled square and circular carbon steel sections with or without concrete infill. For the in-filled specimens, the concrete was unbonded from the tube by greasing the internal tube surface prior to filling with concrete. For square tubes, O'Shea and Bridge [23] found that the change of buckling mode can result in a higher load capacity for the thin-walled steel tube component compared with that for the unfilled bare steel tube. The test results indicate that the strength enhancement increased from 45% when the width-to-thickness ratio B/t was 57 to 67% when B/t was 131. No obvious strength enhancement, however, was found for an in-filled square tube with a B/t ratio of 37. This is because this tube was rather stocky, and the steel could be loaded up to its yield strength [23]. For circular tubes with diameter-to-thickness ratios D/t varying from 59 to 220, O'Shea and Bridge [24] presented that the concrete infill had little effect on the local buckling strength of the steel tube in axial compression. This is due to the "elephant's foot" buckling mode being dominantly outwards which is unaffected by internal restraint.

According to O'Shea and Bridge [23,24], the strength increase for the current specimens in the S series was not as a direct result of the change of buckling mode. This can be verified by checking the corresponding axial strains ε_{max} shown in Fig. 10 and Table 2 when the maximum loads were attained. For all specimens in the H and S series, the stainless steel has reached its yield strength at peak loads and the value of ε_{max} for an in-filled tube was generally larger than that of its corresponding unfilled tube. It seems the concrete's infill allowed the stainless steel to better develop its material behaviour beyond its nominal yield point. This reflects the high non-linearity of stainless steel which is unusual for conventional carbon steel. It should be noted that no specific measures were taken in the current tests to eliminate the bond between the steel tube and concrete. Although the stainless steel inner surface was expected to have a smaller bond strength compared with that

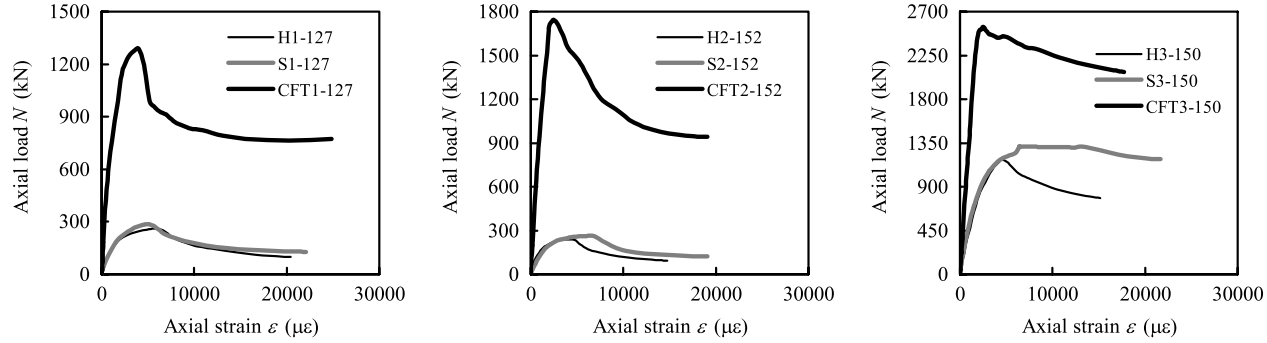

(a) Circular section ($D = 127$ mm). (b) Circular section ($D = 152.4$ mm). (c) Square section.

Fig. 10. Comparison of N–ε curves of stub columns under different loading conditions.

in a carbon steel tube, there is a need to further investigate the influence of bond in the future.

Fig. 10 shows the comparison of N–ε curves for the specimens in different test series. It is clear that the modulus is greatly enhanced for the CFST columns compared with other specimens in the H or S series. Since the concrete's strength was comparatively high, the composite columns demonstrated lower ductility compared with those specimens given in Table 1. The modulus difference in the initial loading stage between the specimens in H and S series is moderate, whilst the residual strengths for the specimens in the S series are obviously higher than those of the empty tubes. This is once again owing to the buckling restriction effect of concrete during the post-buckling loading stage.

3.3. Behaviour of short columns under combined actions

Twelve tests shown in Table 3 were undertaken to investigate the strength of both square hollow tubes and square composite short columns under uni-axial loading combined with bending. The hollow columns were identified by the code of H-t-e, whilst the composite columns were identified by the following code, C-t-e, where t is the nominal thickness of the section in mm and e is the eccentricity of the load from the cross-section centroid. The plate slenderness (B/t) of the specimens varied between 20 and 35, which indicates that all plates can be considered to be compact or stocky. The concrete used had a target strength f_c' of 33 MPa at 28 days. But the measured strength was found to be only 12 MPa because of the low curing temperatures in the winter season.

The failure modes of the composite and hollow columns are shown in Fig. 11. All of the specimens experienced the expected buckling modes. Compared with the axial compressive columns, the eccentrically loaded columns developed a somewhat lateral deflection. Since the columns were quite short, the maximum deflection has not occurred near the specimens' mid-height in most cases. It can also be observed that the local buckling was not developed evenly around the specimens' cross-section owing to the bending effect.

Since the recorded lateral deflection at mid-height was generally small, the axial shortening (Δ) is therefore used to depict the axial load versus deformation curves for those specimens.

Fig. 12 shows the effect of concrete filling on the N–Δ/L curves. Apparently, the influence is generally the same as that described before for the stub columns under axial compression. The hollow columns reached failure at a lower load than the composite columns. The overall strength and stability of the composite columns were enhanced by the concrete's core, especially by denying the steel from buckling inwards and thus avoiding local buckling from occurring before the peak load was reached.

The effect of load eccentricity (e) on the N–Δ/L curves for the composite columns is demonstrated in Fig. 13. The influence of e on the column stiffness is minor when the value of e is small. When e reaches to 40 mm, an apparent stiffness decrease can be found. The load-bearing capacity of the composite columns decreases with increasing load eccentricity. Owing to the utilisation of stainless steel, all composite columns exhibited very ductile behaviour, even after having experienced severe deformation.

3.4. Behaviour of slender columns

Twenty four tests were planned as shown in Table 4, where three kinds of specimens with circular, square and rectangular cross-sections shown in Fig. 1, respectively, were prepared. Other investigation parameters were selected as the concrete's cylinder strength f_c' (36.3, 75.4 MPa), and slenderness ratio λ (15.2–103.5). For circular columns, the effect of diameter-to-thickness ratio D/t (40.6, 68.2) was also investigated. To distinguish specimens with different parameters, the specimen labels are assigned according to (1) section shape (C, S and R refer to specimens with circular, square and rectangular sections, respectively); (2) tube thickness (1 and 2 used to distinguish specimens with different tube thicknesses for circular sections); (3) slenderness ratio (1, 2 and 3 used to distinguish specimens with different slenderness ratios); and (4) concrete strength ("a" for normal strength concrete and "b" for high strength concrete). The above-mentioned slenderness ratio (λ) defined in [25] is used herein

$$\lambda = \frac{L_e}{i} \tag{2}$$

where L_e is the effective length of a column; $i = \sqrt{I_{sc}/A_{sc}}$, is the section radius of gyration, I_{sc} and A_{sc} are the second moment of area and area of the CFST composite cross-section, respectively. Therefore, the slenderness ratios for the composite columns with different cross-sections can be determined by

$$\lambda = 4L_e/D \quad \text{(circular column)} \tag{3a}$$

$$\lambda = 2\sqrt{3}L_e/B \quad \text{(square or rectangular column)} \tag{3b}$$

where D is the overall diameter of a circular column, and B is the overall width of a square or rectangular column.

3.4.1. Test observations

The test results of the columns are summarised in Table 4, where $u_{m,\text{ult}}$ is the mid-height deflection measured at the peak load (N_{ue}), and ε_{cu} and ε_L are the corresponding axial and lateral strains respectively, which were measured from the strain gauges located at the extreme compression fibre.

Fig. 14 shows a general view of typical specimens after testing. It was observed that all slender columns failed in a typical flexural mode with large lateral deflections. For those short columns, their failure was characterised by axial compression. Despite this,

(a) CFST columns.

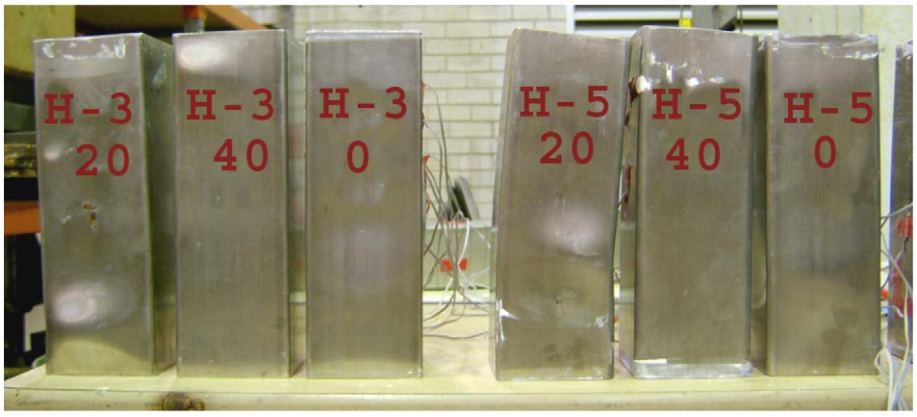

(b) Hollow tubes.

Fig. 11. Failure modes of CFST columns and hollow tubes under combined actions.

obvious bending deformation has also developed at the end of the testing, as can be seen from Fig. 14(a). Since all utilised hollow sections were compact or nearly compact (rectangular section) according to EC4 [10], local buckling was only observed after the peak load had been attained except those slender circular columns without local buckling being observed at all. The local buckling of a steel tube (if any) generally occurred near the specimen mid-height, as shown in Fig. 14.

Lateral deflections were measured along the column's height for those slender specimens. The lateral deformation was not obvious before the peak load was reached. After the peak load had been attained, the lateral deformation developed progressively accompanied by load reduction. For a slender square column, obvious lateral deformation was generally observed in the two perpendicular directions for measurement, whilst a short square column bent predominantly in one direction. Since the second moment of area for a rectangular column about its major axis in the current tests was much bigger than that about its minor axis, the deflection observed was mainly along its major axis. At the initial loading stage, generally, the deflection curve of a specimen was not completely symmetrical owing to the random distribution of initial global imperfections. During the post-peak stage, the deflection curve was approximately in the shape of half-sine wave.

From the above test observations, it seems that there is no obvious difference between CFSST columns and conventional concrete-filled steel tubular columns comprised of carbon steel in terms of test observations and failure modes [26].

3.4.2. Effect of slenderness ratio

The effect of slenderness ratio (λ) on typical axial load (N) versus mid-height lateral deflection (u_m) curves is shown in Fig. 15.

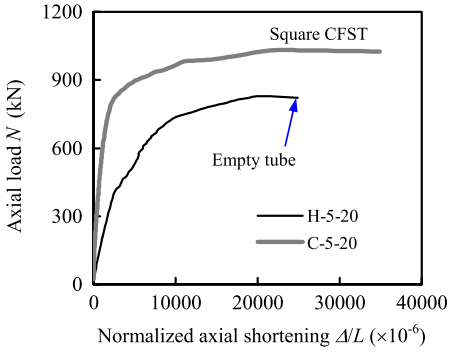

Fig. 12. Effect of concrete filling on N–Δ/L curves.

Since rectangular columns showed the same nature as those square columns in terms of the effect of λ, no curves of rectangular columns are given in Fig. 15. As can be seen, the larger the slenderness ratio, the smaller the peak load is. Also, the post-peak curves generally become steeper with decreasing λ. According to EC4 [10], the shortest columns in each test series have attained their section capacities, whilst those slenderest columns only attained 50.8%–83.5% of their section capacities. It is thus expected that slenderness reduction factors should be applied in designing slender CFSST columns.

Fig. 16 demonstrates the effect of slenderness ratio on the N–Δ/L curves, where Δ is the measured axial shortening, and L is the length of a column. The initial portion of the N–Δ/L curve for a longer column essentially followed the curve of its corresponding shorter column before attaining the peak load.

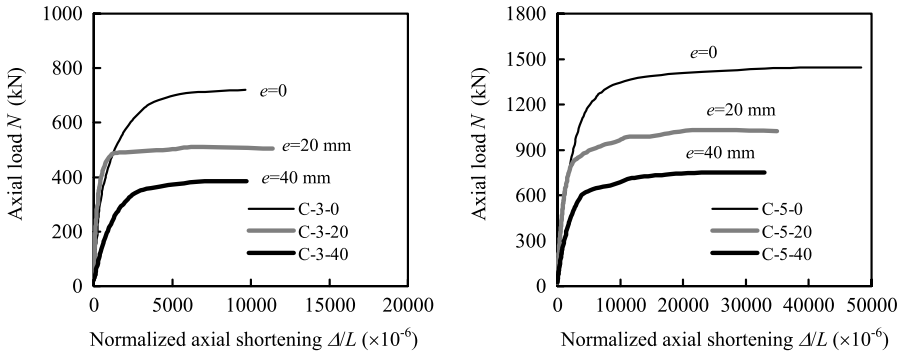

(a) $t = 2.85$ mm. (b) $t = 5.05$ mm.

Fig. 13. Effect of load eccentricity on N–Δ/L curves.

(a) Circular cross-section.

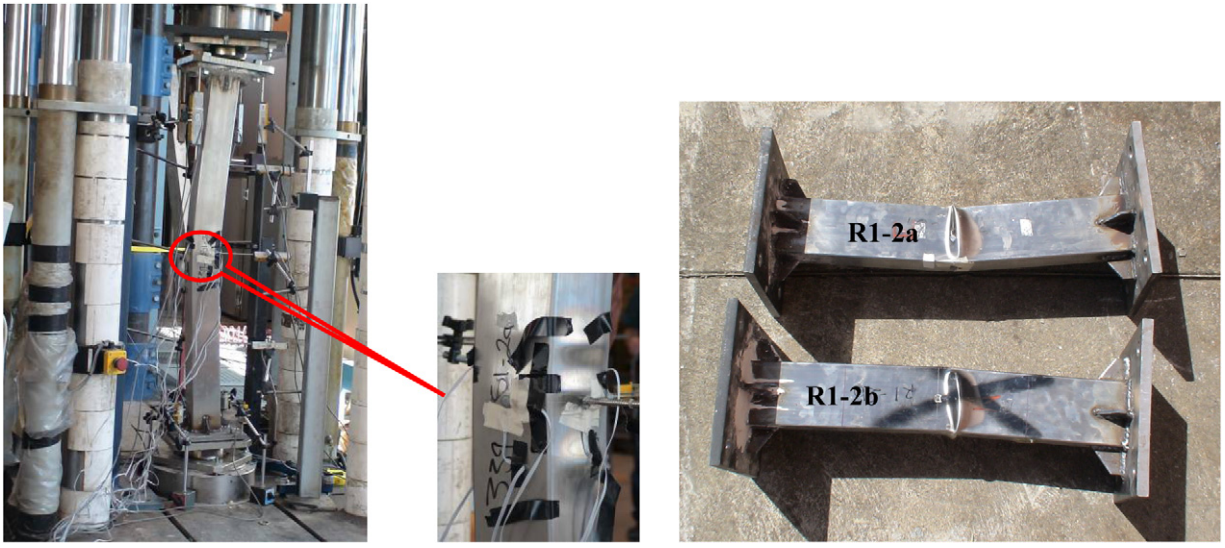

(b) Square cross-section (S1-2a). (c) Rectangular cross-section.

Fig. 14. A general view of typical slender specimens after testing.

The larger the slenderness ratio, the smaller the value of Δ/L at peak load is. This trend is even more obvious for those columns infilled with high-strength concrete. Owing to the influence of global slenderness, only short columns have developed Δ/L at their peak loads with values bigger than or near steel yield strains, as shown in Fig. 16.

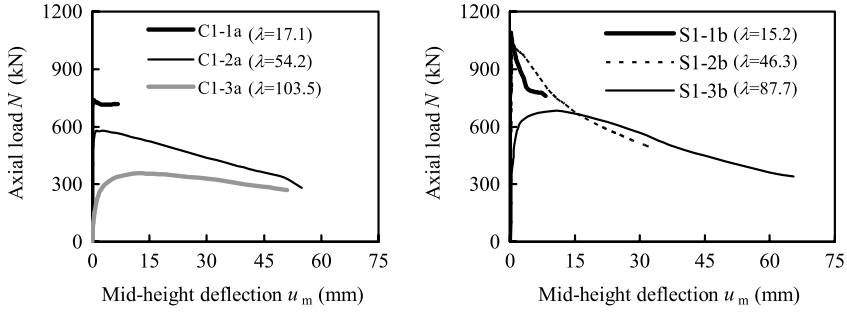

(a) Circular columns ($f_c' = 36.3$ MPa). (b) Square columns ($f_c' = 75.4$ MPa).

Fig. 15. Effect of slenderness ratio on N–u_m curves.

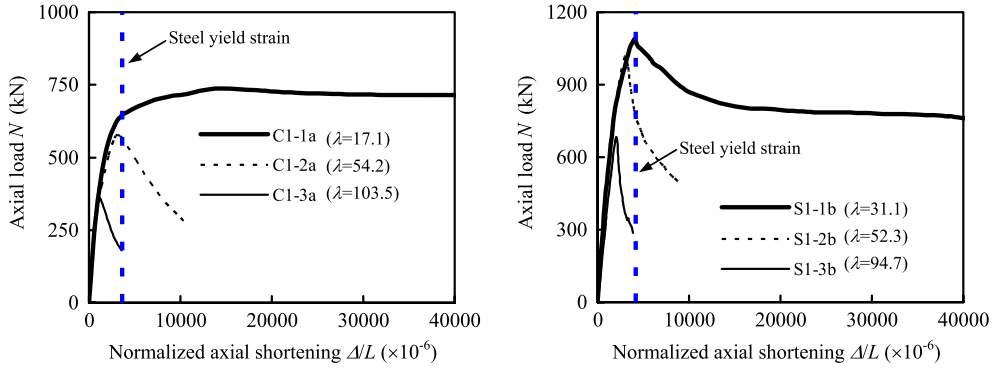

(a) Circular columns ($f_c' = 36.3$ MPa). (b) Square columns ($f_c' = 75.4$ MPa).

Fig. 16. Effect of slenderness ratio on N–Δ/L curves.

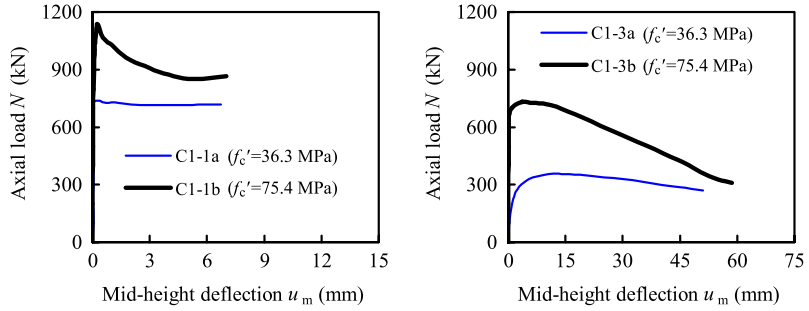

(a) $\lambda = 17.1$. (b) $\lambda = 103.5$.

Fig. 17. Effect of concrete strength on N–u_m curves.

3.4.3. Effect of concrete strength

The compressive strength of the high-strength concrete ($f_c' = 75.4$ MPa) was about two times that of the normal strength concrete with a value of 36.3 MPa. Compared with columns comprised of high-strength concrete, it is not surprising that more ductile behaviour was achieved as normal strength concrete was used, as shown in Fig. 17. This trend is less obvious with an increase of slenderness ratio, owing to the fact that slender columns generally underwent elastic buckling. Thus, the influence of concrete strength is less significant in this case.

3.4.4. Effect of diameter-to-thickness ratio

All circular specimens tested were fabricated from two kinds of steel tubes with different diameter-to-thickness ratios (D/t). The effect of D/t on the N–u_m curves is plotted in Fig. 18. Clearly, specimens with a smaller D/t ratio reveal a more ductile behaviour. But this effect is only apparent for the short columns. It seems that the D/t ratio has no significant influence on the shape of N–u_m curves for those slender columns. This is attributed to the fact that the confinement of steel tube on concrete is less effective with an increasing of slenderness ratio.

3.4.5. Strain analysis

Strain developments for specimens with different tube shapes are quite similar. Therefore, the axial and lateral strain developments are illustrated in Fig. 19 with two typical square specimens S1-1a and S1-3b, where the strains were measured at the columns' mid-height. The strain readings from strain gauges located on different tube surfaces are all shown in these figures, where the axial strain gauges are designated as A1, A2, A3, A4, and the corresponding lateral strain gauges are designated as L1, L2, L3, L4, respectively. As can be seen, the whole section for each column was under compression before the peak load was reached. During this stage, there was no obvious variation among the measured strains at different locations. This demonstrated that the column was under nearly pure compression. After the peak load has been reached, part of the cross-section for a slender column reversed from compression to tension, as shown in Fig. 19(b). This results from the

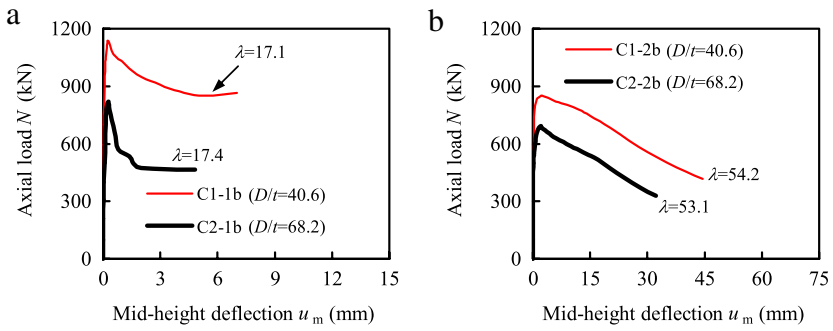

Fig. 18. Effect of diameter-to-thickness ratio on N–u_m curves.

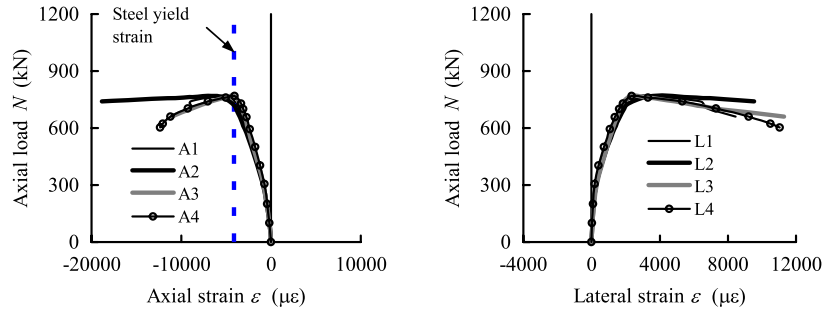

(a) S1-1a ($\lambda = 15.2, f_c' = 36.3$ MPa).

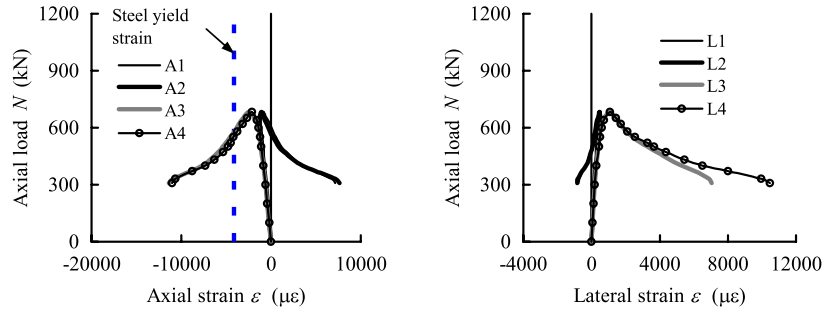

(b) S1-3b ($\lambda = 87.7, f_c' = 75.4$ MPa).

Fig. 19. Axial and lateral strains measured at different tube locations.

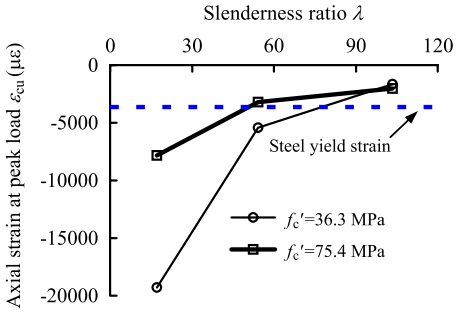

Fig. 20. Effect of slenderness ratio and concrete strength on ε_{cu} (circular columns, $D/t = 40.6$).

more prominent second-order effect and the generation of excess second-order moment.

The effect of slenderness ratio and concrete strength on the ultimate axial strain (ε_{cu}) is shown in Fig. 20. Generally, the value of ε_{cu} decreases with increasing slenderness ratio. This is because a column with a larger slenderness ratio failed at a smaller load level, and the materials had not been fully utilised. From Fig. 20, it can also be seen that a specimen comprised of high strength concrete generally has a smaller ε_{cu} compared with the corresponding specimen in-filled with normal strength concrete. It is not surprising since high-strength concrete dilates much slower under high axial loading than normal strength concrete, thus the confinement effect from steel tube is more pronounced for the normal strength concrete. This is also proved by the comparison of the lateral strains (ε_L) measured at peak loads, as shown in Table 4.

It should be noted that the above trend is not observed for those slenderest columns in each test series. Since those columns underwent elastic buckling, the high-strength concrete with a higher elastic modulus was helpful for a column to gain higher strength and to increase the steel strains.

The lateral-to-axial strain ratios (ν) of a steel tube, which can be used to evaluate the confinement of the concrete offered by the steel tube, were calculated from strain readings with corresponding ultimate strains shown in Table 4. Fig. 21 depicts the development of the lateral-to-axial strain ratios for typical steel coupons, as well as circular and square steel tubes. It is worth noting that the trend for rectangular columns is quite similar to that of square columns. Therefore, no test results are given in Fig. 21 for rectangular columns. To make a meaningful comparison, the axial loads (N) in Fig. 21 are normalized with respect to the corresponding peak loads (N_{ue}). As far as a steel coupon is

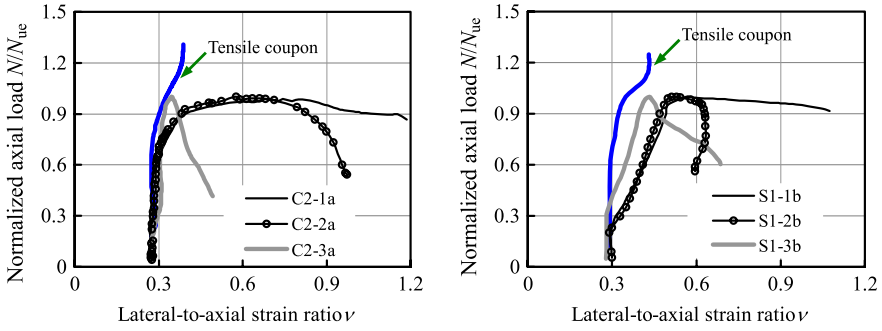

(a) Circular columns. (b) Square columns.

Fig. 21. Development of lateral-to-axial strain ratios for steel coupons and steel tubes.

concerned, its vertical coordinate is replaced by its normalized stress ($\sigma/\sigma_{0.2}$).

The lateral-to-axial strain ratios for all steel tubes shown in Fig. 21 are initially around 0.3, which are virtually the same as those of the steel coupons. Thus, it is concluded that the steel tubes had no confining effect on the concrete at this moment. When the load reached about 60%–80% the peak load, the lateral-to-axial strain ratio for the steel tube in a shorter column increased much faster, and was even larger than 0.5 before the peak load was reached. This is due to the lateral expansion of the concrete, resulting in the confinement from the steel tube. For those slenderest columns in each test series, however, there is no significant increase in the lateral-to-axial strain ratios at the peak loads. It seems that the composite action between the steel tube and the concrete core decreases with increasing slenderness ratio.

From Fig. 21, it can also be found that the lateral-to-axial strain ratio for a square tube increased much faster than that of a circular tube when the load reached about 30% the peak load. This does not mean that the square tube demonstrated higher confinement on the concrete than the circular tube. It seems that the development of lateral-to-axial strain ratio for those square tubes has been affected by the plate bending during the loading process.

4. Comparisons between tests and code predicted strengths

Nowadays, there are several well-known national standards or recommendations to address the design of carbon steel CFST columns [27], such as Australian standard AS 5100 [7], American code AISC [8], Chinese code DBJ/T [9], and EC4 [10]. No standard, however, is now available for the design of CFSST columns. Based on the comprehensive experimental program undertaken in this paper, the design codes are compared with the test results to evaluate their applicability. The material partial safety factors specified in all design codes have been taken as unity when comparing code calculations with the tests. At the same time, all code limitations, such as the limits on concrete strength and steel strength, are ignored with a purpose to check the feasibility of those design codes in predicting the load-carrying capacities of the test specimens.

4.1. Section capacity under axial compression

As shown in Figs. 5–8, the peak loads for some stocky specimens are associated with very high plastic strains. In these cases, the relatively high strains are not of general structural interest. It seems that further research in the future should be done to investigate the definition of load-carrying capacity for sections having Type A or B curves as shown in Fig. 5. In this paper, the loads N_{ue} at a maximum strain limit of 1% have been presented in Table 1 for comparison. If the maximum load $N_{\max}$ (or first peak load) attained below 1% strain, N_{ue} will have a same value as the maximum or first peak load. The axial strains ε_{cu} corresponding to N_{ue} are also given in Table 1.

Figs. 22 and 23 compare the measured maximum loads $N_{\max}$ of the circular and square stub columns respectively with the predicted strength N_{uc} based on different code provisions. It is clear that all codes are conservative in predicting $N_{\max}$, especially for those circular columns. AS 5100 gives the best predictions for circular columns with an average value (μ) of 1.406 for the ratio of $N_{\max}/N_{uc}$ and a standard deviation (σ) of 0.207; whilst the closest predictions for square columns are from DBJ/T ($\mu = 1.242, \sigma = 0.146$). The values of μ and σ for other code predictions are presented in Table 6. From Figs. 22 and 23, there is a declining trend of the $N_{\max}/N_{uc}$ ratios as the section slenderness increases.

Figs. 24 and 25 illustrate the comparison between the measured N_{ue} and the predicted strength N_{uc} for the circular and square stub columns, respectively. All codes give more reasonable predictions for N_{ue} than for $N_{\max}$, though the predictions for N_{ue} are still conservative in general. The average value of $N_{\max}/N_{uc}$ is 32.6% higher than that of N_{ue}/N_{uc} for circular columns, whilst the average values of $N_{\max}/N_{uc}$ and N_{ue}/N_{uc} for square columns are quite close (the average value of $N_{\max}/N_{uc}$ is 5.6% higher). It can also be found from Figs. 24 and 25 that, once again, AS 5100 and DBJ/T give the best predictions for circular and square columns with a μ of 1.078 and 1.175 and a σ of 0.132 and 0.101, respectively.

4.2. Section capacity under combined actions

Fig. 26 compares the predicted axial load (N) versus moment (M) interaction curves with the test results of short columns under uni-axial loading combined with bending, where M is calculated as $N \cdot e$ for the test results. All codes are conservative and underestimate the axial loads by 47%–67%, where DBJ/T gives the closest predictions. Since the predictions are based on the measured maximum loads ($N_{\max}$), it seems that there is further research need to define the load-carrying capacity and develop a more accurate design approach to better utilise the material behaviour of stainless steel.

4.3. Member capacity of slender columns

The comparison between the test results N_{ue} and code predictions N_{uc} is shown in Tables 7 and 8. For brevity, the predicted results using AS 5100, AISC, DBJ/T and EC4 are designated as N_{AS5100}, N_{AISC}, N_{DBJ} and N_{EC4} in these tables, respectively. The obtained average values (μ) and standard deviations (σ) of N_{ue}/N_{uc} for each code prediction are given in Tables 7 and 8. Obviously, all codes are generally conservative and underestimate the columns' strength by about 11.1%–25.5% on average. The predictions for the circular columns are even more conservative than those for the square and rectangular counterparts.

It should be noted that similar comparisons have been made by Tao et al. [27] for conventional circular and rectangular (including

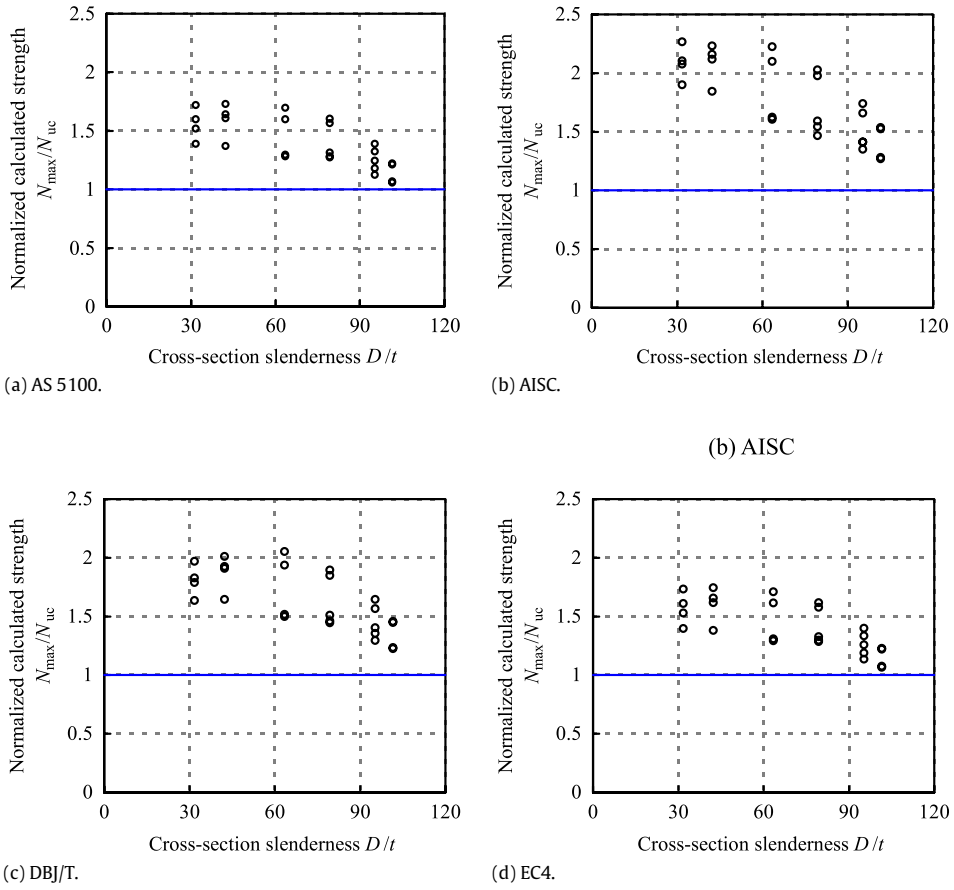

Fig. 22. Comparison between N_{max} and code predictions (circular stub columns).

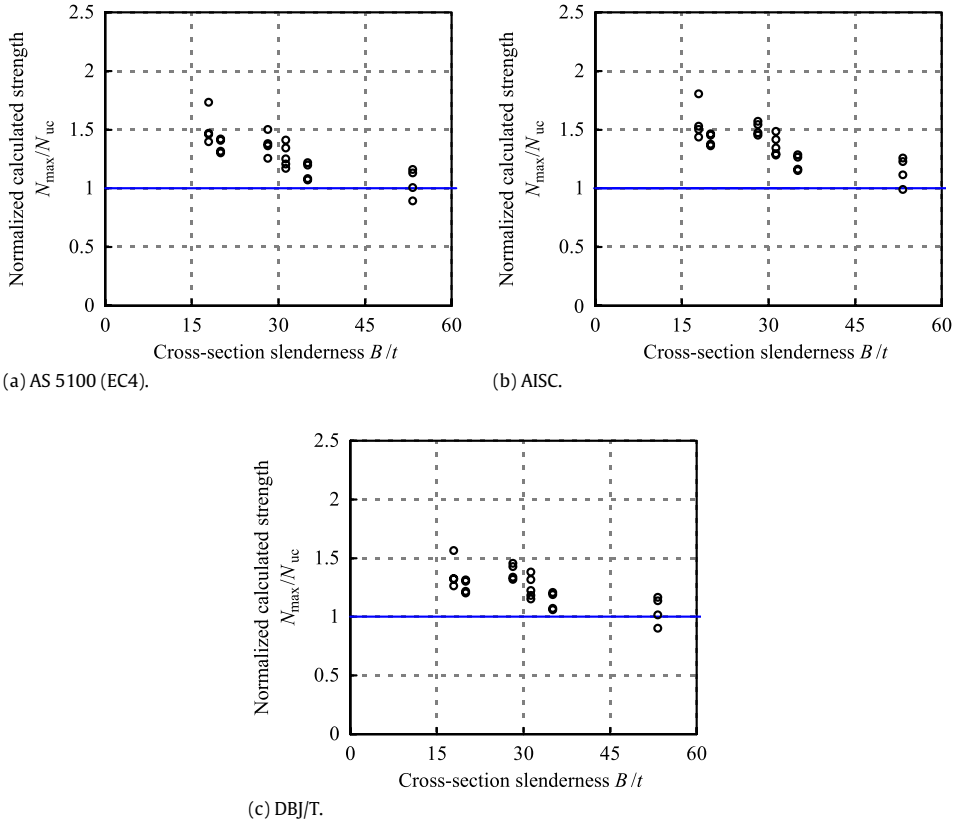

Fig. 23. Comparison between N_{max} and code predictions (square stub columns).

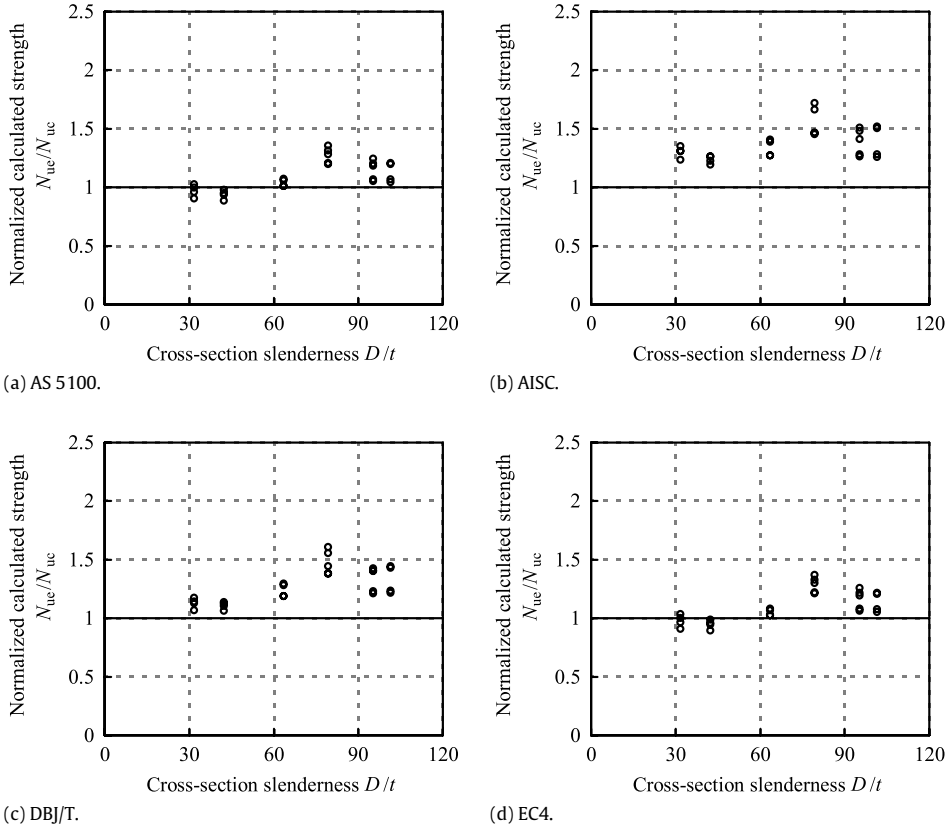

Fig. 24. Comparison between N_{ue} and code predictions (circular stub columns).

Table 6
Comparison results of code predictions with test results of short columns.

Section type	Loading type	AS 5100		AISC		DBJ/T		EC4	
		μ	σ	μ	σ	μ	σ	μ	σ
Circular	Axial loading (N_{max})	1.406	0.207	1.799	0.326	1.653	0.254	1.419	0.209
	Axial loading (N_{ue})	1.078	0.132	1.370	0.137	1.266	0.153	1.088	0.134
Square	Axial loading (N_{max})	1.295	0.185	1.370	0.173	1.242	0.146	1.295	0.185
	Axial loading (N_{ue})	1.223	0.119	1.295	0.108	1.175	0.101	1.223	0.119
	Combined actions	1.519	0.064	1.666	0.099	1.465	0.058	1.595	0.097

square columns) carbon steel CFST columns, where a total of 420 and 234 test results were compared, respectively. After comparing the predictions for CFSST and carbon steel CFST columns, it was found that there is no significant difference in terms of prediction accuracy. However, compared with carbon steel CFST columns, all codes give a little more conservative predictions for the CFSST columns. In general, the prediction differences in μ for the two kinds of column are within 8%.

It should be noted that for carbon steel columns, a codified out-of-straightness value of $L/1000$ is often used for axially compressed slender columns to reflect the influence of initial imperfections and unintended load eccentricity. For stainless steel columns, there is no such specification of a codified out-of-straightness at this moment. For the CFSST columns tested in this paper, it is conceivable that the current codes give conservative strength predictions since these columns were ideally straight and subjected to no intended eccentricity as mentioned before. In general, initial global imperfections for real columns vary randomly depending on different supplied tubes. The range of initial global imperfections is normally from $L/1000$ to $L/10\,000$ based on a literature survey. Further research is needed to recommend a codified out-of-straightness, and to present a suitable design method for CFSST slender columns.

5. Conclusions

A comprehensive experimental investigation of short and slender concrete-filled stainless steel tubular columns has been carried out in this paper. Comparisons of the test results were also made with several existing design methods for conventional concrete-filled carbon steel tubular columns. The following conclusions can be drawn within the limitation of this study:

(1) The axial load versus axial strain curves for CFSST stub columns under pure compression can be classified into three types associated with a strain-hardening or strain-softening response. Compared with conventional carbon steel CFST columns, the stainless steel composite columns show more ductile behaviour and have a much higher residual strength.
(2) Six circular and three square stub columns were investigated to evaluate the influence of different loading methods. Compared with empty tubes, a strength increase was found for the in-filled columns even though only the steel tubes were loaded.
(3) The short composite columns under combined actions of axial force and bending moment exhibited very ductile behaviour. The overall strength and stability of the CFST columns were enhanced by the in-filled concrete.

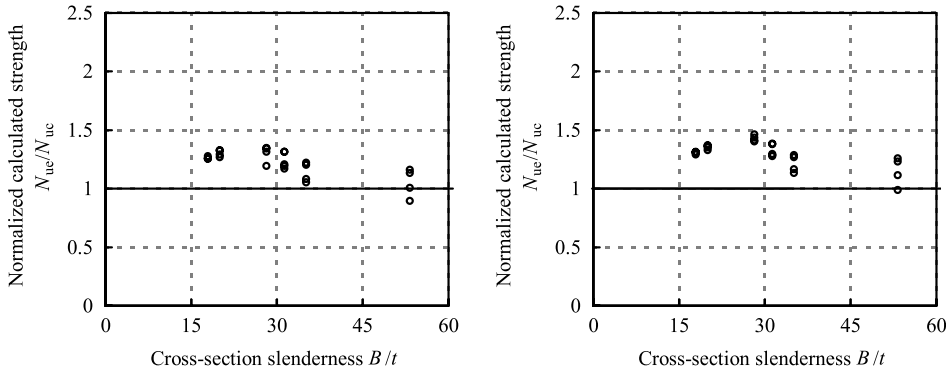

(a) AS 5100 (EC4). (b) AISC.

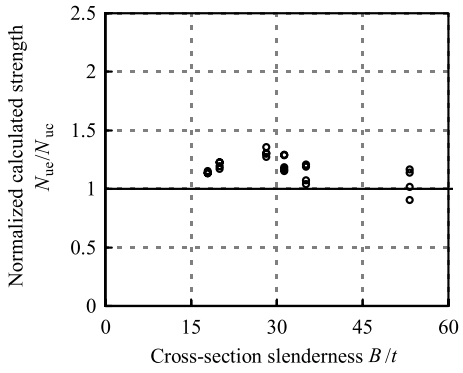

(c) DBJ/T.

Fig. 25. Comparison between N_{ue} and code predictions (square stub columns).

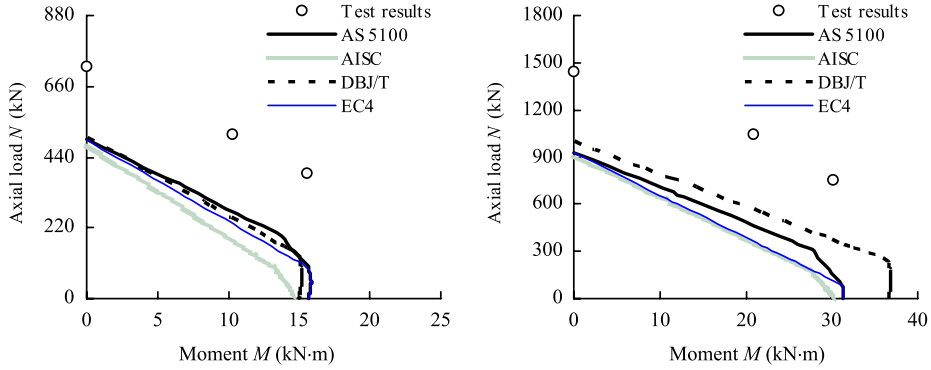

(a) C-3 ($B \times t = 101 \times 2.85$ mm). (b) C-5 ($B \times t = 101 \times 5.05$ mm).

Fig. 26. Comparison of predicted interaction curves with test results.

Table 7
Code predictions for circular slender CFSST columns.

No.	Specimen label	N_{ue}	N_{AS5100}	N_{ue}/N_{AS5100}	N_{AISC}	N_{ue}/N_{AISC}	N_{DBJ}	N_{ue}/N_{DBJ}	N_{EC4}	N_{ue}/N_{EC4}
1	C1-1a	738.0	709.0	1.041	589.6	1.252	642.9	1.148	703.9	1.048
2	C1-1b	1137.1	1038.6	1.095	921.2	1.234	951.1	1.196	1032.4	1.101
3	C1-2a	578.9	532.0	1.088	524.3	1.104	523.5	1.106	549.5	1.053
4	C1-2b	851.1	804.7	1.058	785.2	1.084	708.4	1.201	818.6	1.040
5	C1-3a	357.6	361.2	0.990	371.3	0.963	376.6	0.950	357.8	0.999
6	C1-3b	731.8	476.5	1.536	491.2	1.490	478.9	1.528	426.3	1.717
7	C2-1a	501.3	469.2	1.068	402.4	1.246	419.0	1.196	466.0	1.076
8	C2-1b	819.0	744.0	1.101	674.2	1.215	663.3	1.235	738.1	1.110
9	C2-2a	446.0	364.3	1.224	353.3	1.262	340.5	1.310	373.4	1.194
10	C2-2b	692.9	588.0	1.178	561.9	1.233	492.8	1.406	585.7	1.183
11	C2-3a	383.0	245.6	1.559	242.1	1.582	239.7	1.598	232.8	1.645
12	C2-3b	389.7	342.2	1.139	331.0	1.177	327.1	1.191	284.3	1.371
μ				1.173		1.237		1.255		1.211
σ				0.185		0.166		0.181		0.241

Table 8
Code predictions for square and rectangular slender CFSST columns.

No.	Specimen label	N_{ue}	N_{AS5100}	N_{AS5100}/N_{ue}	N_{AISC}	N_{AISC}/N_{ue}	N_{DBJ}	N_{DBJ}/N_{ue}	N_{EC4}	N_{EC4}/N_{ue}
1	S1-1a	767.6	743.4	1.033	689.7	1.113	735.8	1.043	746.4	1.028
2	S1-1b	1090.5	1081.7	1.008	982.1	1.110	1054.6	1.034	1096.1	0.995
3	S1-2a	697.3	670.6	1.040	628.3	1.110	635.3	1.098	681.3	1.024
4	S1-2b	1022.9	942.6	1.085	874.4	1.170	833.3	1.228	964.4	1.061
5	S1-3a	622.9	481.6	1.293	479.2	1.300	488.8	1.274	488.4	1.276
6	S1-3b	684.2	627.2	1.091	623.7	1.097	600.5	1.139	586.9	1.166
7	R1-1a	385.6	341.5	1.129	322.7	1.195	332.6	1.159	348.7	1.106
8	R1-1b	558.3	494.2	1.130	455.3	1.226	455.3	1.226	504.2	1.107
9	R1-2a	361.1	313.4	1.152	299.3	1.207	298.5	1.210	324.9	1.111
10	R1-2b	517.7	443.7	1.167	413.7	1.251	387.3	1.337	456.4	1.134
11	R1-3a	262.8	228.3	1.151	229.5	1.145	226.9	1.158	234.1	1.123
12	R1-3b	332.8	292.1	1.139	295.1	1.128	278.3	1.196	278.5	1.195
μ				1.118		1.171		1.175		1.111
σ				0.076		0.065		0.089		0.079

(4) For the slender columns, there is no obvious difference between CFSST columns and conventional carbon steel CFST columns in terms of test observations and failure modes. A codified out-of-straightness should be suggested in the future for slender CFSST columns.
(5) All the four codes used in this paper somewhat underestimate the load-carrying capacities of CFSST columns under both axial compression and combined actions. There is further research need to develop a more accurate design approach to better utilise the material behaviour of stainless steel.

Acknowledgements

This work is supported by the Australian Research Council (ARC) under its Future Fellowships scheme (Project No: FT0991433). This research work has also been partially supported by the Research Grant Scheme and the International Research Initiatives Scheme provided by the University of Western Sydney. The financial support is gratefully acknowledged.

References

[1] Mann AP. The structural use of stainless steel. The Structural Engineer 1993; 71(4):60–9.
[2] Gardner L. Aesthetics, economics and design of stainless steel structures. Advanced Steel Construction 2008;4(2):113–22.
[3] Uy B. Stability and ductility of high performancee steel sections with concrete infill. Journal of Constructional Steel Research 2008;64(7–8):748–54.
[4] Young B, Ellobody E. Experimental investigation of concrete-filled cold-formed high strength stainless steel tube columns. Journal of Constructional Steel Research 2006;62(5):484–92.
[5] Lam D, Gardner L. Structural design of stainless steel concrete filled columns. Journal of Constructional Steel Research 2008;64(11):1275–82.
[6] Rasmussen KJR. Full-range stress–strain curves for stainless steel alloys. Journal of Constructional Steel Research 2003;59(1):47–61.
[7] Standards Australia. Bridge design, part 6: steel and composite construction. AS 5100.6-2004. Sydney (Australia); 2004.
[8] ANSI/AISC 360-05. Specification for structural steel buildings. Chicago (IL, USA): American Institute of Steel Construction; 2005.
[9] DBJ/T 13-51-2010. Technical specification for concrete-filled steel tubular structures. Fuzhou (China): The Department of Housing and Urban–Rural Development of Fujian Province; 2010 [in Chinese].
[10] Eurocode 4. Design of composite steel and concrete structures, part 1.1: general rules and rules for building. BS EN 1994-1-1: 2004. London (UK): British Standards Institution; 2004.
[11] Tao Z, Han LH, Wang ZB. Experimental behaviour of stiffened concrete-filled thin-walled hollow steel structural (HSS) stub columns. Journal of Constructional Steel Research 2005;61(7):962–83.
[12] Standards Australia. Cold-formed stainless steel structures. AS/NZS 4673:2001. Sydney (Australia); 2001.
[13] Ashraf M, Gardner L, Nethercot DA. Strength enhancement of the corner regions of stainless steel cross-sections. Journal of Constructional Steel Research 2005;61(1):37–52.
[14] Eurocode 2. Design of concrete structures, part 1.1: general rules and rules for building. BS EN 1992-1-1: 2004. London (UK): British Standards Institution; 2004.
[15] Han LH. The influence of concrete compaction on the strength of concrete filled steel tubes. Advances in Structural Engineering 2000;3(2):131–7.
[16] Quach WM, Teng JG, Chung KF. Three-stage full-range stress–strain model for stainless steels. Journal of Structural Engineering, ASCE 2008;134(9): 1518–1527.
[17] Tao Z, Han LH, Wang DY. Strength and ductility of stiffened thin-walled hollow steel structural stub columns filled with concrete. Thin-Walled Structures 2008;46(10):1113–28.
[18] Han LH, Zhao XL, Tao Z. Tests and mechanics model for concrete-filled SHS stub columns, columns and beam–columns. Steel and Composite Structures 2001; 1(1):51–74.
[19] Han LH, Yao GH, Zhao XL. Tests and calculations of hollow structural steel (HSS) stub columns filled with self-consolidating concrete (SCC). Journal of Constructional Steel Research 2005;61(9):1241–69.
[20] Han LH, Yao GH. Experimental behaviour of thin-walled hollow structural steel (HSS) columns filled with self-consolidating concrete (SCC). Thin-Walled Structures 2004;42(9):1357–77.
[21] Chen ZY, Zhu JQ, Wu PG. High strength concrete and its application. Beijing (China): Tsinghua University Press; 1996 [in Chinese].
[22] Yu Q, Tao Z, Wu YX. Experimental behaviour of high performancee concrete-filled steel tubular columns. Thin-Walled Structures 2008;46(4):362–70.
[23] O'Shea MD, Bridge RQ. Behaviour of thin-walled box sections with lateral restraint. Research report no. R739. Sydney (Australia): Department of Civil Engineering, the University of Sydney; 1997.
[24] O'Shea MD, Bridge RQ. Local buckling of thin-walled circular steel sections with or without internal restraint. Research report no. R740. Sydney (Australia): Department of Civil Engineering, the University of Sydney; 1997.
[25] Han LH, Tao Z, Huang H, Zhao XL. Concrete-filled double skin (SHS outer and CHS inner) steel tubular beam–columns. Thin-Walled Structures 2004;42(9): 1329–55.
[26] Han LH. Tests on concrete filled steel tubular columns with high slenderness ratio. Advances in Structural Engineering 2000;3(4):337–44.
[27] Tao Z, Uy B, Han LH, He SH. Design of concrete-filled steel tubular members according to the Australian standard AS 5100 model and calibration. Australian Journal of Structural Engineering 2008;8(3):197–214.